Astron. Astrophys. 321, 754–764 (1997)

ASTRONOMY
AND
ASTROPHYSICS

The ringed, warped and isolated galaxy NGC 6015⋆

L. Verdes-Montenegro[1], **A. Bosma**[2], **and E. Athanassoula**[2]

[1] Instituto de Astrofísica de Andalucía, CSIC, Apdo. 3004, E-18080 Granada, Spain
[2] Observatoire de Marseille, 2 Place le Verrier, F-13248 Marseille Cedex 4, France

Received 14 August 1996 / Accepted 25 October 1996

Abstract. We have studied the neutral hydrogen component of the ringed and unbarred Scd galaxy NGC 6015 with the Westerbork telescope at a resolution of $13.6'' \times 15.4''$ ($\alpha \times \delta$) and a velocity resolution of 33 km s^{-1}. These data have been supplemented with CCD-BVRI surface photometry and optical spectroscopy.

The study of the stellar and HI gas component of NGC 6015 shows that its structure changes from small to large radii. In the inner $60''$ there is a blue two armed spiral structure, previously measured by Elmegreen and Elmegreen. In the following $30''$ the pattern changes to a flocculent one. At $90''$ two pseudoarms start, the outer parts winding in a blue pseudoring $153\farcs1 \times 56\farcs1$ in size. About 41% of the HI emission is concentrated in this ring. The extent of the HI gas is about twice that of the optical emission, and an analysis of the HI distribution and velocity field indicates that NGC 6015 is warped at radii larger than $170''$. In the inner parts the velocity field can be modelled well by normal circular rotation in a disk of the same extent as the optical one.

Assuming, as is known to be the case for barred galaxies, that the outer pseudoring is at the outer Lindblad resonance, we derive a value for the pattern speed of 26.5 km s^{-1}kpc^{-1}. The expected locations for the other resonances then follow from the combined optical/HI rotation curve, and in particular we find that the end of the inner spiral structure is located at the ultraharmonic (4:1) resonance, in agreement with the result found by Patsis et al. for Sb and Sc type galaxies.

Key words: galaxies: spiral; kinematics and dynamics; structure; NGC 6015 – radio lines: galaxies

1. Introduction

The formation of rings and pseudorings is thought to be associated with orbital resonances produced in non-axisymmetric mass distributions (Schwarz 1981; Athanassoula et al. 1982; Schwarz 1984a, b, c, 1985; Buta, 1986; Buta & Crocker 1991), and indeed, they are mostly found in early type barred galaxies (cf. Buta 1995). There are, however, isolated galaxies with rings in which no sizeable bar or oval component can be seen. In order to understand the formation of rings in such objects, we have started a detailed study of the gaseous and stellar component of isolated non-barred galaxies with outer rings. Such studies might reveal the existence of weak deviations from axisymmetry, e.g. ovals, or point to other mechanisms involved in the formation of these rings. In a previous paper (Verdes-Montenegro et al., 1995, hereafter Paper I) we present HI observations, CCD imaging and spectroscopy of the galaxy NGC 7217 and conclude that the location of its three rings is consistent with that of resonances due to a bi-symmetric pattern. However, we have not been able to clearly identify the feature responsible for setting up this pattern, and discuss elsewhere scenarios in which a bar was present in this galaxy, and responsible for the rings, but disappears due to an increase in the central concentration of the galaxy, thereby leaving the rings, and creating a retrograde population of stars. (cf. Athanassoula, 1996, and Athanassoula et al. 1996).

Here we report the results of HI line emission and CCD-BVRI photometry and Hα spectroscopy of the galaxy NGC 6015, classified as SA(s)cd by de Vaucouleurs, et al (1991). Although outer rings in such late type spirals are very rare, NGC 6015 is not unique, and more cases exist, such as NGC 3684 (Sandage & Bedke 1994). We list in Table 1 the main parameters of NGC 6015. The distribution of its HII regions has been studied by García-Gómez & Athanassoula (1993) and described as rather clumpy and irregular, with no clear spiral arms. De Vaucouleurs & Buta (1980b) have measured from optical emission a diameter for the pseudoring of $\sim 5\farcm2 \times 1\farcm8$.

Prieto et al. (1992ab) made a photometric CCD-BRIZ study of the central parts of NGC 6015, out to a radius of $80''$ while B and I semi-major axis profiles extending to $160''$ are available from Elmegreen & Elmegreen (1984). Carozzi (1976) shows a rotation curve out to $90''$, and finds that the velocities are still increasing at that distance. HI integrated spectra have been obtained by many authors, e.g. Tifft & Cocke (1988) with a beam of $\simeq 10\farcm8$. The CO(2-1) and CO(1-0) emission lines have

Send offprint requests to: L. Verdes-Montenegro

⋆ Based partially on data collected at the Observatoire de Haute Provence, France

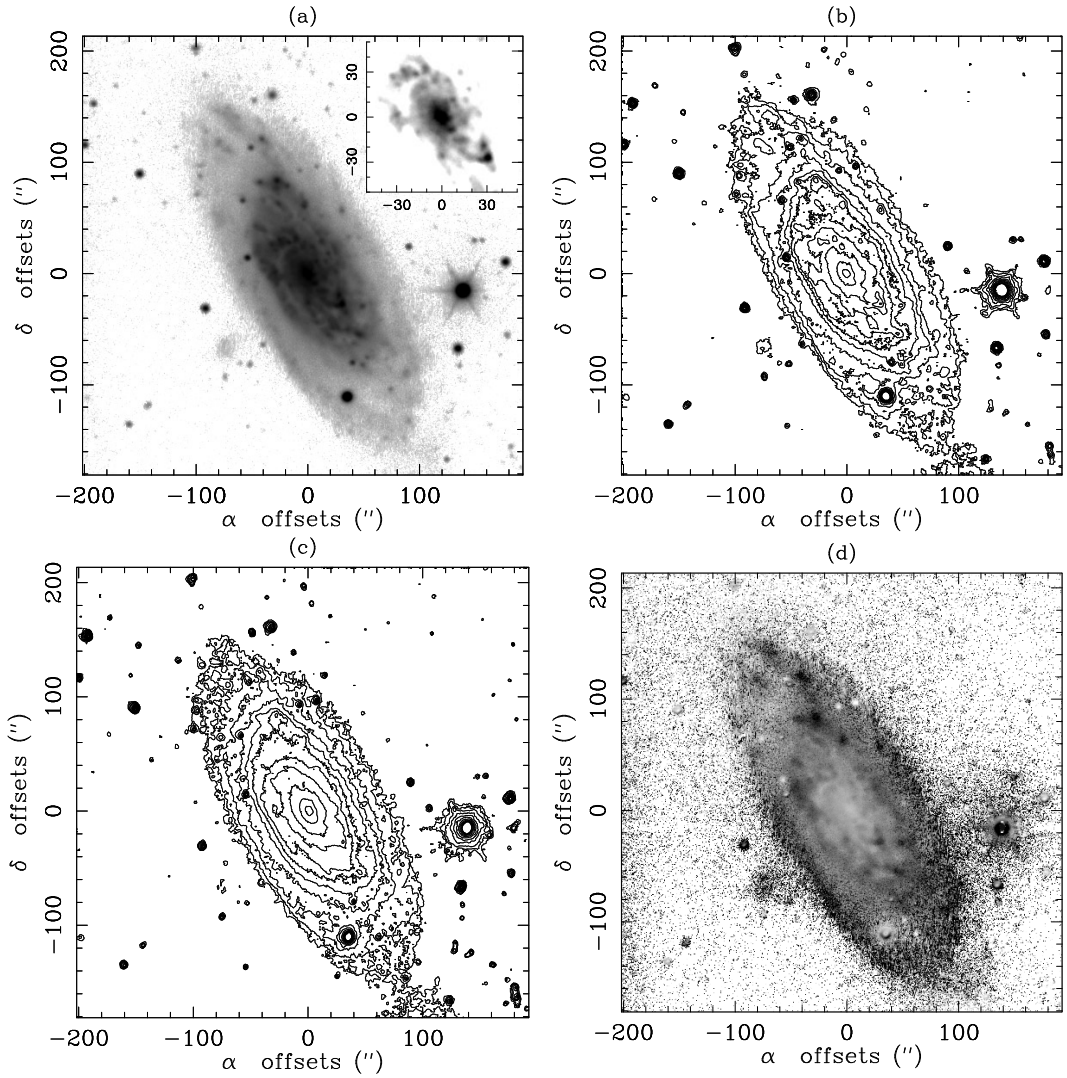

Fig. 1. a B image of NGC 6015 in a logarithmic grey scale representation. Higher intensities are darker. A close up of the central region is shown in the upper right, where the inner spiral structure is evident. **b** Isophotal contours corresponding to the V filter image, ranging from 19.5 to 24.5 mag/($''$)^2, with a step of 0.5. **c** Isophotal contours corresponding to the I filter image, ranging from 18.5 to 23.5 mag/($''$)^2, with a step of 0.5. **d** B-R colour image in a grey scale where black is bluer and white is redder. Colours have been corrected for interstellar absorption as explained in Sect. 2.1. The orientation of all the images is North up and East to the left.

been detected by Braine et al. (1993) with the IRAM 30-m radiotelescope (beam $\simeq 12''$ and $23''$ respectively) toward the central parts of the galaxy.

The systemic heliocentric radial velocity of this galaxy, obtained from our HI data and corrected to the centroid of the Local Group is 1045 km s^{-1}. A Hubble constant of 75 km s^{-1} Mpc^{-1} gives a distance of 13.9 Mpc. After inspection of both the CfA redshift survey and the NED[1] database we find that the nearest bright galaxy is NGC 5949 at an apparent separation of 3.6 degrees (projected separation of 875 kpc at the distance of NGC 6015), a velocity of 649 km s^{-1} and 1 magn. fainter than NGC 6015. NGC 6140 is 4.8 degrees away from NGC 6015 (1.1 Mpc), has a velocity of 1124 km s^{-1} and a similar magnitude. Three dwarf galaxies exist also at projected distances of 245 kpc, 486 kpc and 1.2 Mpc, with radial velocities w.r.t. the Local Group centroid of, respectively, 1112, 1084 and 874 km s^{-1}.

[1] The NASA/IPAC extragalactic database (NED) is operated by the Jet Propulsion Laboratory, California Institute of Technology, under contract with the National Aeronautics and Space Administration

2. Observations and data analysis

2.1. Photometry

We obtained CCD images of NGC 6015 in the BVRI bands at the Newtonian focus of the 1.20 m telescope of the Observatoire de Haute Provence (France) using a Tektronix CCD camera with 512×512 pixels, and a scale of 0.″77/pixel. The exposure times were 15 minutes in B and 5 minutes in V, R and I each. The

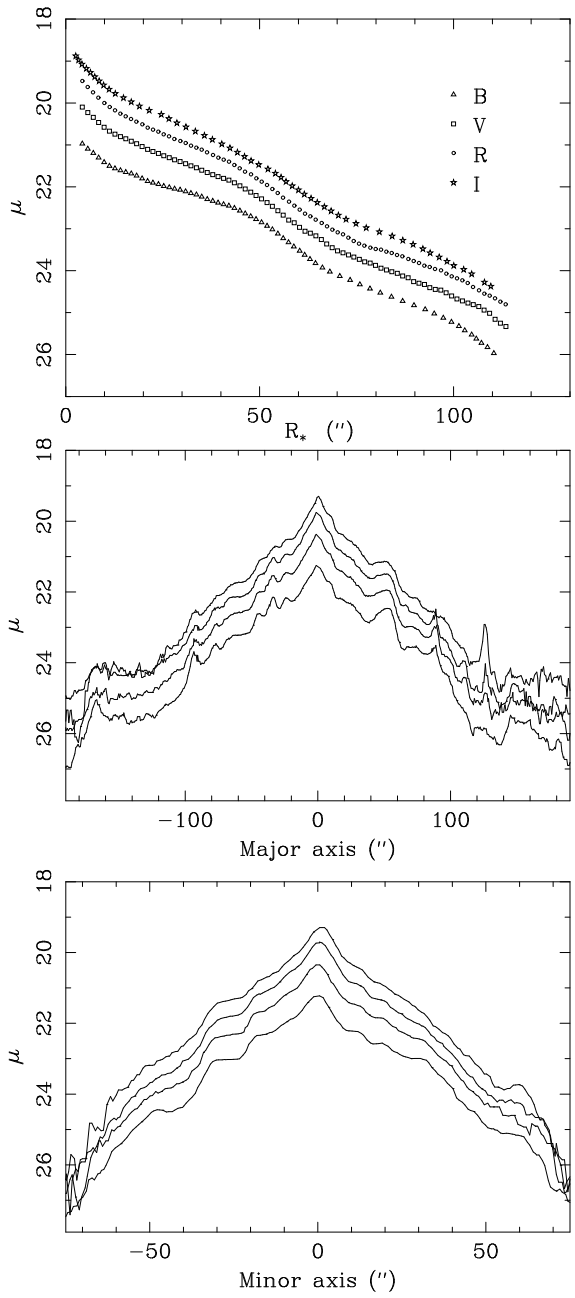

Fig. 2. a Averaged radial profiles in each individual photometric pass band as a function of the equivalent radius of each isophotal level. **b** Major axis profile cuts for B, V, R and I filters from down to up. **c** The same as in **b** for minor axis.

seeing of each frame was measured from the FWHM obtained by fitting a two dimensional analytic Moffat function to the projected stars in the field of the group. It amounts to 3.″0 in B, 2.″9 in V, 2.″5 in R and 2.″2 in I. The reduction and calibration of the data were performed in a standard way. The atmospheric extinction was determined through observations of the open cluster M92, and the rms errors in the standard stars in the final calibration are smaller than 0.16 mag for B, 0.06 mag for B-V, 0.08 mag for V-R, and 0.05 for R-I. Data reduction and analysis were made as in Paper I. Colours have been corrected for galactic foreground absorption using the extinction value given by Burstein and Heiles (1984), with the reddening law from Savage & Mathis (1979), and for internal extinction with A_i = 0.59 (de Vaucouleurs et al. 1991).

2.2. Optical spectroscopy

Long slit spectroscopy around the wavelength of Hα has been obtained with the 1.93 m telescope of the Observatoire de Haute Provence, using the Carelec spectrograph equipped with a Tektronix CCD camera with 512×512 pixels. The slit length is about 5.8 arcmin, and the spectral resolution was 33 Åmm^{-1}. Data were taken at position angles 208°, 188°, 228°, and 118°. The data were reduced in a standard manner, and emission line velocities were determined from the Hα-line, the [NII]-lines and the [SII]-lines. The data near the minor axis (118°) do not indicate large scale deviations from circular motions. The data at position angles 188°, 208°, and 228° were analyzed together using a minimization routine. From this we determined the best fitting values for the spatial orientation parameters, its systemic velocity, and a rotation curve in the central parts of the galaxy.

2.3. Radio observations

Observations of the 21 cm line of HI were made with the Westerbork Synthesis Radio Telescope (WSRT[2]) during 1983. We used 40 interferometers with spacings ranging from 36 m to 2700 m in steps of 72 m. This results in a synthesized beam of 13.″6 × 15.″4 ($\alpha \times \delta$) and first grating response at 10′ × 11.3′ ($\alpha \times \delta$). We used a digital backend (Bos et al. 1981) resulting in 31 channel maps at heliocentric velocities 586.7 to 1081.3 km s^{-1}. Hanning smoothing was applied on-line, giving a velocity resolution of 33.0 km s^{-1}.

The data were edited and calibrated as explained in Paper I. A rms noise level of $\sim$ 0.8 mJy/beam was achieved after 12 hours of integration. To get a higher signal-to-noise ratio in the integrated HI distribution and associated radial velocity field, we convolved the map data with a gaussian, leading to a beam size of 25.″0 × 25.″0 ($\alpha \times \delta$) and rms of 0.5 mJy/beam. Primary beam corrections have been applied to our maps.

3. Results

3.1. Optical emission

In Fig. 1a we present a logarithmic grey scale representation of the B band image of NGC 6015. A close-up of the inner part is shown in the upper right corner, with a different grey level representation. There it can be seen that two spiral arms exist for 40 $\lesssim$radius $\lesssim$60″ (see Sect. 4.3), which were previously identified by Elmegreen & Elmegreen (1995). A dense set of

[2] The Westerbork Synthesis Radio Telescope is operated by the Netherlands Foundation for Radio Astronomy with financial support from the Netherlands Foundation for the Advancement of Pure Research (Z. W. O.)

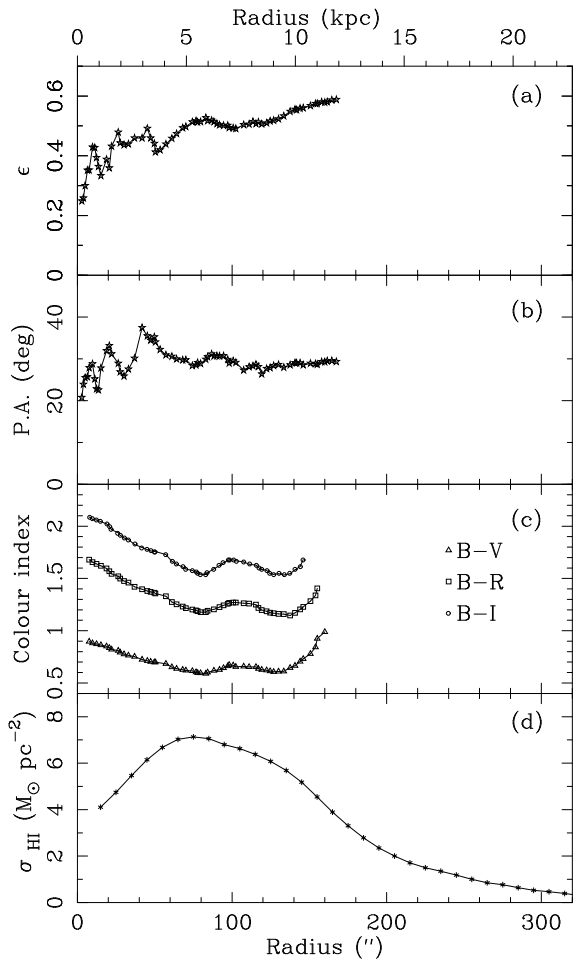

Fig. 3. a Ellipticity, **b** position angle of the ellipses fitted to the isophotes as a function of their semimajor axis length (see §3.1). **c** Radial colour index profiles (B-I, B-V and B-R) obtained by integrating the corresponding images in elliptic annuli of 3″ width and with the geometrical parameters corresponding to the I isophotes. Angles are measured from N to E. **d** The same as **c** for the HI surface density. The lower radial scale is in arcsec and the upper one in kpc, for D = 13.9 Mpc.

flocculent spiral arms is evident for larger radii until a radius of $\sim$ 90″. Two pseudoarms detach from this to the NNE and E from the center, wound counter clockwise. A third arm might also exist to the SSW. There is an increase of emission in the southern edge of the galaxy, produced by two bright stars located close to our frame. In Fig. 1b and c we show the isophotal maps corresponding to the V and I bands. The outer pseudoring, clearly visible on a photograph in the Sandage and Bedke (1994) atlas, can be seen in Fig. 1d, where we present our B-R colour index image. We have preferred B-R to B-I since our R image is deeper and allows to detect light for larger radii, where the outer pseudoring of NGC 6015 is located. It seems to consist of a wide (cross section $\sim$ 20″) blue strip (<B-R> = 1.0), with the more intense emission extending from 80° $\leq$ p.a. $\leq$ 340°. The outer arms seem to end there. In particular the region where the eastern pseudoarm reaches the ring shows enhanced blue colours (<B-R> = 1.5). The geometrical parameters of the pseudoring obtained from the B-R image, together with its characteristic colour indices corrected for galactic foreground absorption are listed in Table 2. The size and orientation of the pseudoring are similar to those measured by de Vaucouleurs & Buta (1980b).

In Fig. 2 we plot the radial brightness profiles for the four observed bands as a function of the equivalent radius (r^*, defined as the radius of a circle having the same area delimited by the isophote) of the corresponding isophotal level. They have been obtained in the same way as explained in Paper I. The profiles show two light excess, increasingly pronounced as we go from I to B. One of them ranges from r^* = 15″ to 65″ and is produced by the bulk of the flocculent spiral arms, and the other one starts at r^* = 75″ and extends at least until the end of our measured profile, containing the outer pseudoring together with the outer pseudoarms. These features, together with the high inclination of the galaxy, prevent an accurate disk-bulge decomposition of the radial profiles. We have made a tentative fit to the less perturbed I-profile, obtaining μ_d = 20.0 mg $(″)^{-2}$ and r_d^* = 37″ for the disk, and μ_b = 24.3 and r_b^* = 6″ for the bulge. The small size obtained for the bulge is consistent with the late morphological type of this galaxy. In Fig. 2b and c we plot cuts along the minor and major axis of the galaxy. From our B image, by extrapolation of a fixed-ellipse averaged profile, we have derived B_T, as listed in Table 1.

Ellipticities and position angles of the ellipses fitted to the isophotes are shown respectively in Fig. 3a and b, as a function of their semimajor axis length. In order to determine the position angle of the disk, we have rejected the values obtained for the central part of NGC 6015 (radius $\leq$ 90″), which are contaminated by the flocculent spiral structure. For larger radii (radius $\geq$ 90″) the position angle remains quite constant, and therefore we have adopted the mean value p.a. = 29.0° $\pm$ 0.4°. The inclination has been obtained from the data between 90″ and 110″ radius, where the ellipticity remains quite constant (0.51 $\pm$ 0.01) and could be fairly attributed to an unperturbed disk component. At radii larger than 110″, where the outer pseudoring and pseudoarms are located, ellipticities increase continuously from 0.49 to 0.59. The adopted value for the ellipticity is equivalent to an inclination of the galaxy to the line of sight of 62°.8 $\pm$ 1°.

The radial colour index profiles, B-V, B-R and B-I are plotted in Fig. 3c. They have been obtained by integrating the two-dimensional colour distribution (Fig. 1d) in elliptic annuli of 3″ width and with the geometrical parameters corresponding to the I isophotes, since the smoother light distribution of the I band image allows a more accurate fitting. Colour indices decrease continuously from the center to the outer parts of NGC 6015 with three blue bumps. The first one, at radius $\simeq$ 50″, corresponds to the inner spiral structure, the second one, at radius $\simeq$ 80″, to the flocculent arms and associated HII regions and the other to the pseudoring that extends for radius $\geq$ 110″. The signal-to-noise ratio of our data is insufficient to determine the colour index radial distribution beyond radii larger than 160″ .

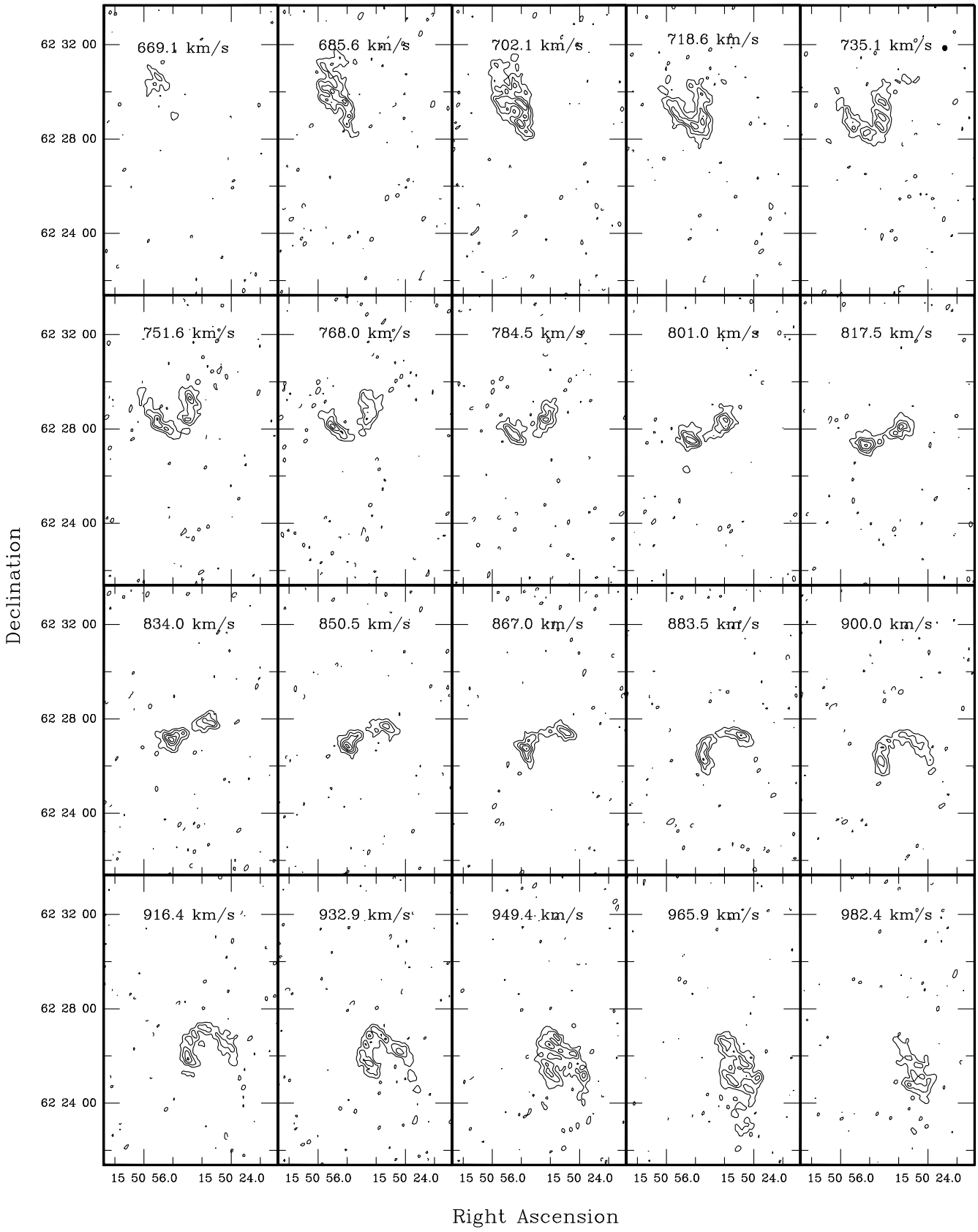

Fig. 4. Channel maps of the 21 cm line radiation. The heliocentric velocities are as indicated in each panel. Contours correspond to -6.3, 6.3, 12.6, 18.9, 25.2 and 31.5 K, and the rms noise of the maps is 2.3 K. The synthesized beam ($13\farcs6 \times 15\farcs4$ - $\alpha \times \delta$) is plotted in the upper right panel.

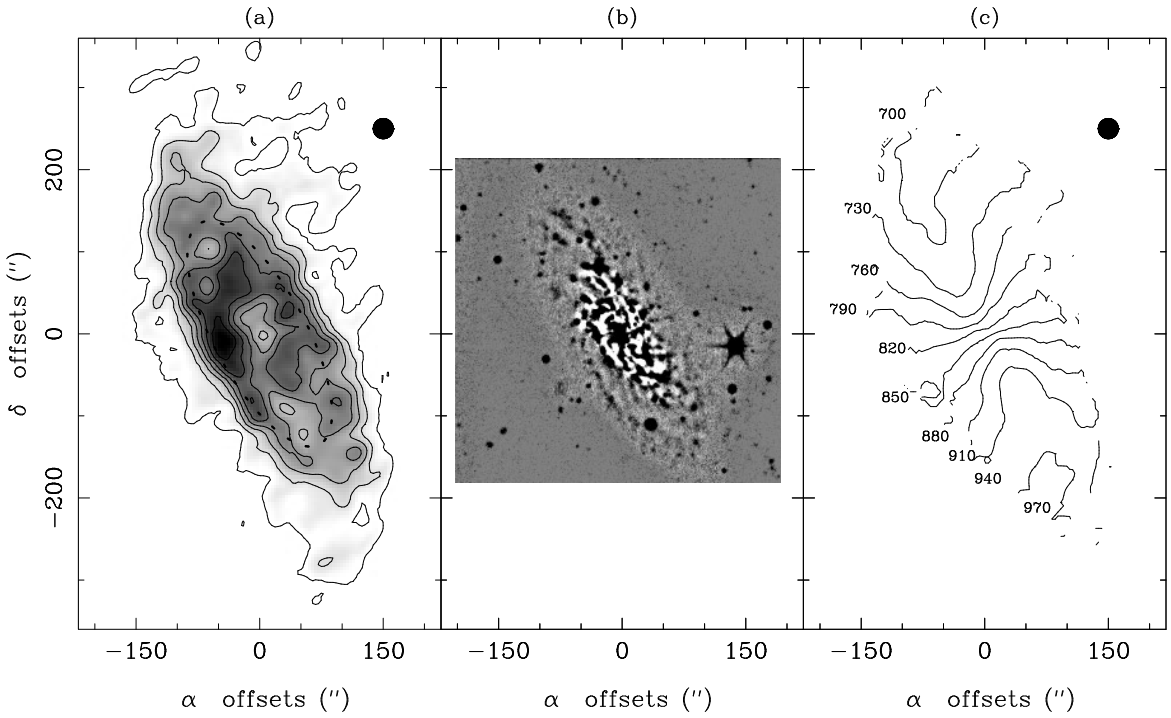

Fig. 5. a Map of the HI column density distribution in NGC 6015. The dashed line corresponds to the ring fitted to the optical B-I image as explained in Sect. 3.1. The contour interval is 3.4×10^{20} atoms cm^{-2}, and the first contour corresponds to 1.7×10^{20} atoms cm^{-2}. Synthesized beam = 25.″0 × 25.″0 ($\alpha \times \delta$). **b** Sharpening of the B image shown in Fig. 1a obtained by the subtraction of a 20″ × 20″ box median filtered image. Darker areas correspond to excess emission. **c** Map of the first-order moment of the radial velocity field. The numbers indicate heliocentric velocities in km s^{-1}. Synthesized beam = 25.″0 × 25.″0 ($\alpha \times \delta$).

Table 1. Parameters of NGC 6015.

Centre position[a]	
α(1950.0)	$15^h\ 50^m\ 39\overset{s}{.}66$
δ(1950.0)	62° 27′ 29.″47
Inclination[b]	63°
Position angle[b]	29°
B_T [c]	11.00
B_T^o [c]	10.38
R_{25} [c]	135″ (9.1 kpc)
Systemic heliocentric velocity	
Optical[c]	834 km s^{-1}
HI[c]	833.4 km s^{-1}
HI[d]	834 km s^{-1}
Distance[c]	13.9 Mpc

[a] Central position of NGC 6015 obtained from our B image.
[b] Obtained from our data as explained in Sect. 3.1.
[c] This paper.
[d] Tifft & Cocke 1988

3.2. 21 cm continuum emission

The channel maps free of line emission were averaged into a map of the continuum radiation and cleaned. Condon (1987) detected at 1.49 GHz a source with a peak flux of 4 mJy associated with the optical centre (cf. Table 1) of NGC 6015. Although this is above our noise level, it cannot be seen in our map because its position is contaminated by the lobe of a bright source located outside our field.

We have found an unresolved continuum source with an integrated flux density of 108 mJy ± 0.8 mJy. Its position (α(1950) = $15^h\ 50^m\ 26\overset{s}{.}98$, δ(1950) = 62° 29′ 35.″6) is coincident, within the beam, with that found by Condon (1987) at 1.49 GHz and Visser et al. (1995) at 151 MHz in their search for extragalactic sources.

Table 2. Ring parameters

Semimajor axis (″)	Semiminor axis (″)	Pos. angle (°)	B-V	B-R	B-I
153.1	56.1	28.3	0.3-0.7	0.6-1.5	0.9-1.7

3.3. Channel maps and integrated emission

In Fig. 4 we display the full resolution channel maps containing the detected HI emission at the observed radial velocities, with a channel width of 16.5 km s^{-1}. The rms noise of the channels is 2.3 K, implying a level of 6.5×10^{19} at cm^{-2} per channel. These channel maps deviate for the outer parts from the usual pattern of inclined spiral galaxies in differential rotation. The orientation of the contours changes as a function of radius

consistently with a warped disk. The atomic gas distribution is slightly asymmetric at low levels; the emission extends more in the major axis direction for the blueshifted channels (i.e. to the NE) than for the redshifted ones.

In order to obtain the integrated HI column density distribution the channel maps were smoothed with a gaussian tapering function (see §2.2) and manually "blotted" to exclude regions of sky where no emission was detectable. Then we added up those pixels in the channel maps where the emission intensity exceeds the r.m.s. noise (1σ) in these blotted and smoothed channel maps. In Fig. 5a we show a contour representation of the total HI column density distribution of NGC 6015. We show also for comparison a "sharpened" B image (Fig. 5b), obtained by the subtraction of a $20'' \times 20''$ median filtered B image, so that the enhanced pseudospiral features can be compared with the atomic gas distribution.

The radius of the atomic gas at 1.5×10^{20} cm^{-2} ($287''$) is 2.1 times more extended than the R_{25} of the optical emission ($135''$ in B). As already noticed in the individual channel maps, at low levels the atomic gas is slightly more extended to the NE part of the galaxy. The warp of the HI disk is apparent in Fig. 5, and will be characterized by using the velocity field in Sect. 3.4. A relative HI depression ($\sim 57\%$ of the peak HI surface intensity) exists in the central $30''$ of the galaxy, as has been observed in many other galaxies. The higher column densities occur at the position of the eastern spiral arm (Fig. 5a). We have plotted on the HI map an ellipse defining the optical pseudoring, and it can be seen that, within the resolution of the HI observations, a large mass of the atomic gas seems also to concentrate there. This is more clearly noticed in Fig. 3d, where we show the radial distribution of the HI column density. It has been obtained by integrating the two-dimensional HI distribution (Fig. 5a) with the geometrical parameters as obtained from the HI velocity field (see Sect. 3.4.). For the radii where the optical emission has been detected we have checked that adoption of the geometrical parameters corresponding to the I isophotes does not change significantly the profile. Therefore direct comparison with Fig. 3a, b and c can be done. The HI ring is evident as a bump in the profile, and starts at a radius similar to its optical counterpart, as seen in Fig. 5a.

The global HI profile is shown in Fig. 6, and was obtained by integrating the flux density in each channel map over an area containing the line emission. It shows a typical two horned shape. The emission is stronger at 700km s^{-1} ($S_\nu \sim 0.45$ Jy) than at its symmetrical velocity, 950km s^{-1}, ($S_\nu \sim 0.37$ Jy). This is due to the excess emission associated to the above described eastern spiral arm (Fig. 4 and 5). The global flux is similar to the one obtained by Tifft and Cocke (1988) with single dish HI observations (see Table 3). It indicates that little atomic gas is located outside the outer pseudoring, and that we did not miss significant extended HI emission in our maps. From this profile we have estimated a total HI gas content of the disk component of 3.4×10^9 M$_\odot$. This mass is of the same order as that obtained by other authors from single dish observations (see Table 3).

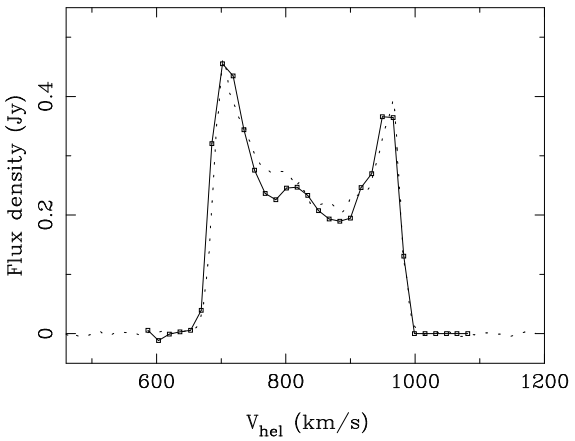

Fig. 6. HI flux density of NGC 6015 as a function of heliocentric velocity. The HI profile from Tifft and Cocke (1988) is plotted with a dotted line for comparison.

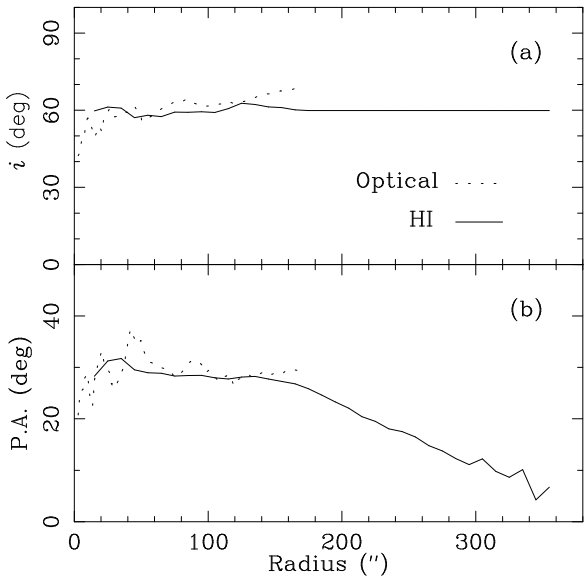

Fig. 7. a Inclination and **b** position angle of NGC 6015 obtained from the fitting of a tilted ring model to the HI velocity field (Sect. 3.4.) are shown as a solid line. The dotted lines correspond to the result for the isophotal fitting of the optical I image. Angles are measured from North to East.

3.4. HI velocity field and rotation curve

Fig. 5c shows the intensity weighted mean radial velocity field, obtained in a similar manner as the total integrated emission (see §3.3). We have fitted a tilted ring model to the velocity field (see Begeman 1987, the ROTCUR task in Gipsy). For the central position we have adopted the position given by our photometry with an accuracy of $0''.7$, $\alpha(1950) = 15^h\ 50^m\ 39^s.66$, $\delta(1950) = 62^\circ\ 27'\ 29''.47$. The central velocity of the integrated HI spectrum at half maximum intensity, 835 km s^{-1}, has been used as initial value for the systemic velocity.

Table 3. Derived parameters

H_I flux[a]	86.0 Jy km s^{-1}
H_I flux[b]	86.7 Jy km s^{-1}
M^a_{HI}	3.9×10^9 M$_\odot$
M^b_{HI}	4.0×10^9 M$_\odot$
M_{HI}/L^0_B [a]	0.16
M_{bulge} (out to 9.1 kpc) [a]	2.3×10^8 M$_\odot$
M_{disk} (out to 9.1 kpc) [a]	2.4×10^{10} M$_\odot$
M_{gas} (out to 9.1 kpc) [a]	2.5×10^9 M$_\odot$
M_{halo} (out to 9.1 kpc) [a]	1.8×10^{10} M$_\odot$

[a] This paper
[b] Tifft & Cocke 1988

We have first studied the central parts of the galaxy (radius $< 170''$) by averaging the approaching and receding part for the calculation of the rotation curve. Points within a sector of $\pm$ 30° from the minor axis were excluded from the fits. The derived systemic velocity is the same as the initial value, 833.4 $\pm$ 0.8km s^{-1}. The isovelocity contours are consistent with a flat galaxy in differential rotation, with an orientation similar to the optical disk. The derived position angle and inclination, with values of 28.3° $\pm$ 0.9° and 59.9° $\pm$ 1.3° respectively are in very good agreement with those obtained from our optical images (p.a. = 29.0° and i = 62.8°). From our optical spectroscopy, we find for the position angle of the major axis 29° $\pm$ 1°, the inclination 58° $\pm$ 1°, and the systemic velocity 834 $\pm$ 1 km s^{-1}, again in good agreement with the HI data and the photometry.

In Fig. 7 we compare values for the position and inclination angle as a function of radius. For larger radii the velocity field cannot be described by the simple picture of an axisymmetric disk in differential rotation. The position angle of the kinematical major axis twists when going outwards. This twisting is similar to the change in orientation of the contours in the integrated HI emission, and in a retrograde sense with respect to the spiral structure. In this region the determination of the inclination is subject to large errors. We have adopted i = 61.5° and obtained the change of the position angle of its major axis (Fig. 7) with errors of the order of 1°. We have calculated separate rotation curves for the approaching and receding halves, as well as for the disk as a whole, as shown in Fig. 8.

We have also constructed a rotation curve based on our optical data. This curve has higher values than the HI curve for the inner 125″. These differences can be explained by beamsmearing: the integration effect is such that the radial velocities are always biased towards values lower than the true values corresponding to the rotation curve (see also Fig. 9 below). We thus combined the optical and radio data into one curve, by adopting the optical data out to 105″ and the HI data for 125″. One point in between has been added to assure a smooth continuation. The result is summarized in Table 4, where the errors reflect the errors in the mean. The larger errors of the velocities for the outer parts are due to the difficulty to obtain an accurate value for the inclination. Even the drop-off at radius 280″ could be spurious, and due to our assumption of constant inclination here. Higher sensitivity observations are needed to investigate the structure of the HI warp in NGC 6015 in a more satisfactory manner. In Fig. 9 we show a position-velocity diagram oriented along the major axis (p.a. = 29°) of the inner disk, where we have overplotted the rotation curve obtained as described above. Since the outer disk is warped, the diagram is not cutting the galaxy through its line of nodes beyond 135″.

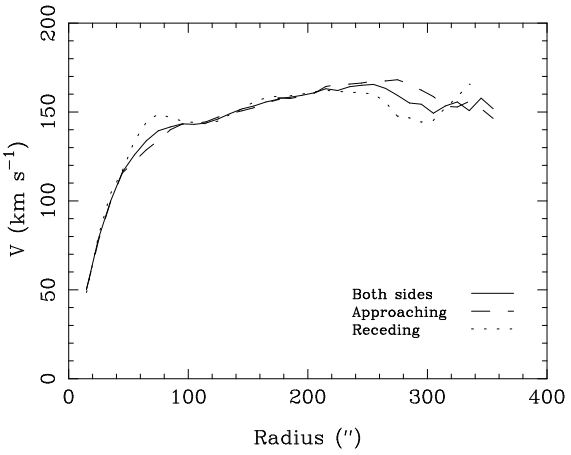

Fig. 8. HI rotation velocity derived from the HI velocity field assuming circular motions. The solid line correspond to the curve derived for both sides of the galaxy. Dashed and dotted ones correspond respectively to the approaching and receding side rotation curves derived independently.

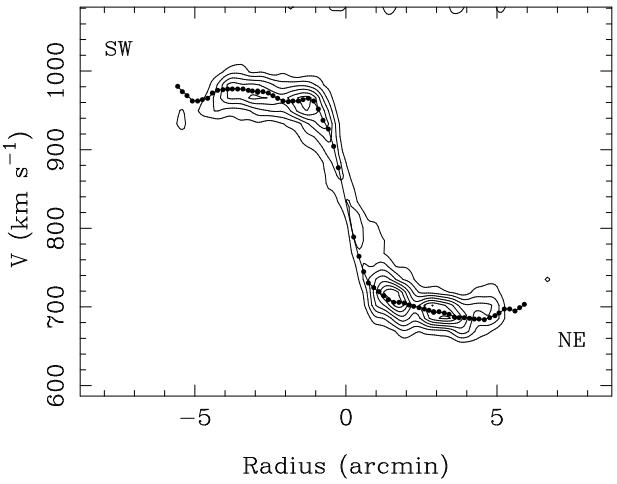

Fig. 9. Position-velocity diagram obtained across the major axis direction. The plotted levels are 0.96, 1.92, 2.88, 3.84, 4.80, 5.76, and 6.72 K, and the noise level 0.48 K. Synthesized beam = 25.″0 × 25.″0 ($\alpha \times \delta$). The dots correspond to the combined optical and radio rotation curve obtained from our data.

4. Discussion

4.1. Rotation curve and mass model

We have constructed a mass model for NGC 6015 based on our photometric data and the combined optical/HI rotation curve

Table 4. Rotation curve

Radius (arcsec)	Rot. velocity (km/s)	r.m.s. error (km/s)	Radius (arcsec)	Rot. velocity (km/s)	r.m.s. error (km/s)
4.1	35.5	2.1	145	151.7	2.8
8.1	62.4	4.2	155	153.4	2.4
12.1	90.7	3.8	165	155.7	2.2
16.1	104.0	2.0	175	157.6	2.8
20.1	104.6	2.4	185	158.3	3.1
24.1	108.1	2.0	195	159.4	3.8
28.1	115.9	2.3	205	160.7	3.6
31.9	129.8	3.3	215	163.0	4.0
35.9	141.2	2.2	225	162.1	4.8
39.8	146.0	1.6	235	164.2	5.7
43.8	149.8	1.4	245	165.0	7.0
47.8	152.1	1.1	255	165.5	6.3
51.8	154.9	1.3	265	163.2	7.0
55.8	152.5	1.8	275	159.3	8.5
60.0	149.7	2.4	285	155.1	9.1
64.2	146.6	5.5	295	154.4	8.0
68.2	145.4	3.8	305	149.3	5.4
72.2	152.1	4.1	315	153.4	3.1
76.1	149.3	1.4	325	155.6	3.0
100	149.0	4.0	335	150.7	9.4
125	146.1	4.0	345	157.8	7.7
135	149.1	3.2	355	151.9	3.4

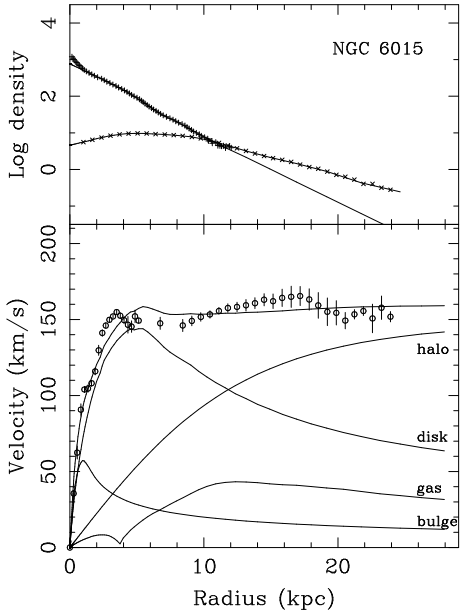

Fig. 10. Composite bulge/disk/gas/halo mass model for NGC 6015. In the top panel the radial distributions of the stellar (plusses) and gas (crosses) components are given in units of $M_\odot$ pc^{-2}. In the bottom panel the rotation curves are shown for each of the components (labelled curves), the best fitting total curve, and the observed rotation curve (circles with error bars, cf. Table 4).

(see Athanassoula et al. 1987 for an extensive description of the mass model procedures). From our I photometric radial luminosity profile, assuming constant mass-to-light ratios for bulge and disk separately, we calculate the expected rotation curve for the luminous mass of the galaxy. We have thus calculated a maximum disc solution with no m = 1, which we show in Fig. 10. For the gas, we correct for helium with a factor 1.36, but we do not correct for molecular hydrogen, which is assumed to follow the light distribution. The resulting mass-to-I-luminosities not corrected for absorption are 4.0 for the bulge, and 1.15 for the disk, which fall within the range found by Athanassoula et al. (1987) for a galaxy of morphological type Scd. The core radius of the halo is 14.0 kpc, its central density 0.0071 $M_\odot$ pc^{-3} and its velocity dispersion 91.6 km s^{-1}. The ratio of halo core radius to optical radius is thus of order 1.5. According to the statistics in Bosma (1991) concerning the frequency of warps, such a large ratio is consistent with NGC 6015 being warped. Further details from the mass model are collected in Table 3.

4.2. Inner spiral structure

As shown in Fig. 1 a spiral structure is present in the inner parts of NGC 6015, which was previously noticed by Elmegreen & Elmegreen (1995). In order to characterize it we have calculated and compared the Fourier components m = 1,..,4 for elliptical annuli of 3″ thickness and deprojected with the position angle and axial ratio calculated above for the galaxy (Sect. 3.1 and 3.4) as a function of radius. They are shown in Fig. 11a, where it can be seen that the m = 2 component, that corresponds to the spiral pattern, peaks in the range $\simeq$ 40″ to 55″ (marked with vertical lines in the figure), and dominates the rest of the components. The phase of this component measured from east counterclockwise changes smoothly from 120° to 150°. The arms can be followed in the B image for $\simeq$ 5″ more, although the m = 2 Fourier amplitude becomes smaller there.

4.3. Outer pseudoring

The outer pseudoring of NGC 6015 is bluer than the rest of the disk (Fig. 1d), probably indicating aggregation of gas that enhances star formation. In fact 43% of the total HI mass (1.5 $\times$ 10^9 $M_\odot$) is contained in the HI counterpart of the optical pseudoring, i.e., between 7.4 and 12.8 kpc.

We have investigated several ways to determine the true spatial form of the outer ring. Deprojection of the galaxy with a position angle of 29° and an ellipticity of 0.51, as derived from the optical image, gives for the pseudoring as seen in B-R an intrinsic axial ratio of q = 0.75. An alternative is to take into account the increase of ellipticity for the outer parts of the optical disk, probably due to the warping of the outer optical disk. We think that this gives a more appropriate value for the intrinsic axial ratio of the pseudoring. Since the local ellipticity of the disk is 0.58 at the radius of the ring, this gives an intrinsic axial ratio for the pseudoring of q = 0.87. This is a normal value for a typical outer feature, as found by Buta (1995) for his sample of southern ringed galaxies.

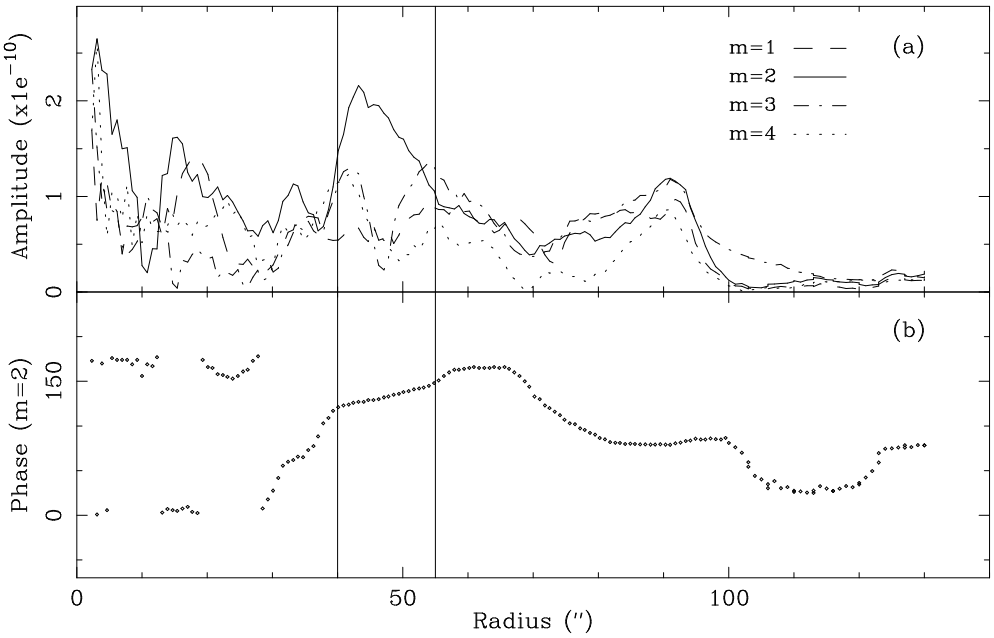

Fig. 11. a Amplitudes of Fourier m=1 to 4 components derives as a function of radius from an analysis of the B image of NGC 6015 deprojected with a position angle of 29° and inclination of 62.8°. The corresponding phase for mode m=2 is plotted in **b**.

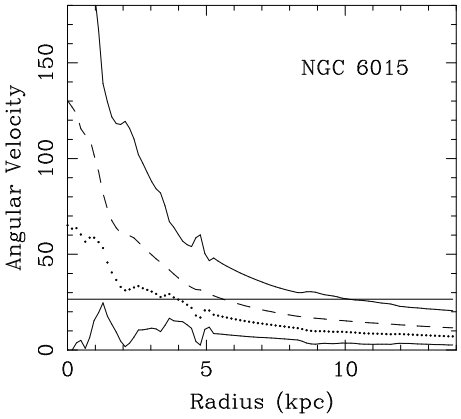

Fig. 12. Angular velocities as function of radius derived from the fitted curve in Fig. 10 : shown are Ω - $\kappa/2$ (lower full drawn curve), Ω - $\kappa/4$ (dotted curve), Ω (dashed curve) and $\Omega + \kappa/2$ (upper full drawn curve). The straight line corresponds to a pattern speed of 26.5 km s^{-1} kpc^{-1}.

4.4. Resonances

Coincidence of the outer ring with the outer Lindblad resonance (OLR) has been deduced in many studies for barred galaxies (Athanassoula et al., 1982, Buta 1986, Buta and Crocker 1991). We will consider this possibility for NGC 6015 also, although we have not found any bar or oval in this galaxy. For the also unbarred galaxy NGC 7217 (Paper I), we have shown however that the identification of its outer ring with the OLR lead to the correspondence of the other two rings with the inner Lindblad resonance and ultraharmonic resonance, respectively. If we accept that the outer pseudoring of NGC 6015 corresponds to the OLR, we can derive the expected locations of the other resonances from the rotation curve. In Fig. 12 we have plotted the computed curves $\Omega + \kappa/2$, Ω, Ω - $\kappa/4$ and Ω - $\kappa/2$ as a function of radius, where Ω is the circular angular velocity and κ is the epicyclic frequency. A location of the OLR at the outer ring position of 10.3 kpc implies a pattern speed of 26.5 km s^{-1} kpc^{-1}, the corotation radius at 5.6 kpc, and the ultraharmonic resonance (UHR, or 4:1 resonance) at 4.0 kpc. Therefore it places the 4:1 resonance at the end of the detected spiral structure (Fig. 1 and Sect. 3.1. and 4.3). This is in agreement with the result found by Contopoulos and Grosbϕl (1986) who show, from the study of periodic orbits in stellar disks, that in normal spiral galaxies spiral arms may terminate near the 4:1 resonance. Patsis et al. (1991) applied such calculations to a set of normal spiral galaxies, finding that in Sb and Sc galaxies the best self-consistent model is the nonlinear model ending at the 4:1 resonance, while in the Sa galaxies the spiral arms end at corotation. We notice here that NGC 6015 is an Scd galaxy. Patsis et al. (1994) extended this result to gaseous disks, by calculating the response of gas, as modelled by SPH, to an imposed spiral pattern. They find that in their best models spirals end at the 4:1 resonance, while a weak ring is seen around the ILR. It would be worthwhile to apply such models to NGC 6015, since that could explain the observed morphology, with the inner spiral arms and their ending point, the intermediate multiarmed spiral region, and the outer ring.

5. Concluding remarks

From our study it appears that the outer ring in NGC 6015 is due to another mechanism than the one operational in barred

spirals. No bar or oval has been found in this galaxy. Its outer ring and inner spiral structure seem to constitute the response to a resonance pattern of $\Omega = 26.5\,\mathrm{km\,s^{-1}\,kpc^{-1}}$ which places them at the OLR and 4:1 resonance, as predicted by some non self-consistent models published in the literature. This intriguing coincidence still leaves open the question why outer rings are relatively rare in ordinary spirals. More work on this topic seems to be warranted.

Acknowledgements. LV-M acknowledges the hospitality and financial support of the Observatoire de Marseille, where part of this work was carried out, and helpful discussions with Dr. A. del Olmo. LV-M is partially supported by DGICYT (Spain) Grant PB93-0159 and Junta de Andalucía (Spain).

References

Athanassoula, E., 1996, in Barred galaxies, I.A.U. Coll. 157, eds. R. Buta, D. Crocker & B.G. Elmegreen, A.S.P. Conf. Series 91, p. 309
Athanassoula, E., Bosma, A., Crézé, M., Schwarz, M. P. 1982, A&A107, 101
Athanassoula, E., Bosma, A., Guivarch, B., Verdes-Montenegro, L., 1996, in New Light on Galaxy evolution, IAU Symp. 171, eds. R. Bender & R.L. davies, (Kluwer, Dordrecht), p. 339.
Athanassoula, E., Bosma, A., Papaioannou, S. 1987, A&A179, 23
Begeman, K. 1987, Ph. D. thesis, University of Groningen
Binney, J. 1991, in Dynamics of disc galaxies, ed. Sundelius, 297
Binney, J. 1992, ARA&A, 30, 1
Bos, A., Raimond, E., van Someren Greve, H. W., 1981, A&A98, 251
Bosma, A. 1991, in Warped Disks and Inclined Rings around Galaxies, ed. S. Casertano, P. D. Sackett, & F. H. Briggs (Cambridge: Cambridge Univ. Press), 181
Braine, J., Combes, F., Casoli, F., Dupraz, C., Gérin, M., Klein, U., Wielibinski, R., Brouillet, N. 1993, A&AS97, 887
Burstein, D., Heiles, C. 1984, ApJS54, 33
Buta, R. 1986, ApJS61, 631
Buta, R. 1995, ApJSS, 96, 39
Buta, R., Crocker, D. A. 1991, AJ102, 1715
Carozzi, N. 1976, A&A49, 425
Condon, J.J. 1987, ApJS65, 485
Contopoulos, G., Grosbϕl, P. 1986, A&A155, 11
de Vaucouleurs, G. 1975, ApJS 29, 193
de Vaucouleurs, G., Buta, R. 1980a, ApJSS 44, 451
de Vaucouleurs, G., Buta, R. 1980b, AJ85, 637
de Vaucouleurs, G., de Vaucouleurs, A., Corwin, H. G., Buta, R. J., Paturel, G., Fouqué, P. 1991, Third Reference Catalogue of Bright Galaxies, Springer, Berlin
Elmegreen, D. M., and Elmegreen, B. G. 1984, ApJS54, 127
Elmegreen, D. M., and Elmegreen, B. G. 1995, ApJ445, 591
García Gómez, C., Athanassoula, E. 1993, A&AS100, 431
Patsis, P. A., Contopoulos, G., Grosbϕl, P. 1994, A&A243, 373
Patsis, P. A., Hiotelis, N., Contopoulos, G., Grosbϕl, P. 1994, A&A286, 46
Pierce, M.J., Tully, R.B. 1992, ApJ387, 47
Prieto, M., Beckman, J. E., Cepa, J., Varela, A. M. 1992a, A&A257, 85
Prieto, M., Longley, D. P. T., Perez, E., Beckman, J. E., Varela, A. M., Cepa, J., 1992b, AASS 93, 557
Roberts, M. S., Haynes, M. 1994, ARAA 32, 115
Sandage, A., Bedke, J. 1994, The Carnegie Atlas of Galaxies, Carnegie Institution, Washington
Savage, B. D., Mathis J. S. 1979, *ARAA* 17, 73
Schwarz, M. P. 1981, ApJ247, 77
Schwarz, M. P. 1984a, A&A133, 222
Schwarz, M. P. 1984b, MNRAS, 209, 93
Schwarz, M. P. 1984c, Proc. Astr. Soc. Australia, 5, 464
Schwarz, M. P. 1985, MNRAS, 212, 677
Savage, B. D., Mathis J. S. 1979, *ARAA* 17, 73
Tifft, W. G., Cocke, W. J. 1988, ApJS67, 1
Verdes-Montenegro, L., Bosma, A., Athanassoula, E. 1995, A&A300, 65
Visser, A. E., Riley, J. M., Röttgering, H. J. A., Waldram, E. M. 1995, A&AS110, 419

This article was processed by the author using Springer-Verlag LaTeX A&A style file *L-AA* version 3.